A High Energy Density Li-ion Battery Cathode Using Only Industrial Elements

Eshaan S. Patheria,[†] Pedro Guzman,[‡] Leah S. Soldner,[†] Michelle D. Qian,[†] Colin T. Morrell,[†] Seong Shik Kim,[†] Kyle Hunady,[‡] Elena R. Priesen Reis,[‡] Nicholas V. Dulock,[†] James R. Neilson,[¶] Johanna Nelson Weker,[§] Brent Fultz,[‡] and Kimberly A. See[*,†]

[†]*Division of Chemistry and Chemical Engineering, California Institute of Technology, Pasadena, California 91125, United States*

[‡]*Department of Applied Physics and Materials Science, California Institute of Technology, Pasadena, California 91125, United States*

[¶]*Department of Chemistry, Colorado State University, Fort Collins, Colorado 80523-1872, United States*

[§]*Stanford Synchrotron Radiation Lightsource, SLAC National Accelerator Laboratory, Menlo Park, California 94025, United States*

E-mail: ksee@caltech.edu

Abstract

Li-ion batteries are crucial for the global energy transition to renewables, but their scalability is limited by the supply of key elements used in commercial cathodes (e.g., Ni, Mn, Co, P). Therefore, there is an urgent need for next-generation cathodes composed of widely available and industrially scalable elements. Here, we introduce a Li-rich cathode based on the known material Li_2FeS_2, composed of low-cost elements (Al, Fe, S) that are globally mined and refined at industrial scale. The substitution of redox-inactive Al^{3+} for Fe^{2+} achieves remarkably high degrees of anion redox, which in turn yields high gravimetric capacity ($\approx$450 mAh·g^{-1}) and energy density ($\gtrapprox$1000 Wh·kg^{-1}). We show that Al^{3+} enables high degrees of delithiation by stabilizing the delithiated state, suppressing phase transformations that would otherwise prevent deep delithiation and extensive anion redox. This mechanistic insight offers new possibilities for developing scalable, next-generation Li-ion battery cathodes to meet pressing societal needs.

Introduction

It is estimated that between 100 to 400 TWh of energy storage are needed to decarbonize/electrify global transport and energy sectors by 2050.[1–3] To achieve that goal with commercial Li-ion batteries with $LiNi_xMn_yCo_zO_2$ (NMCxyz) cathodes, Ni and Co production must double their respective maximum historical compound annual growth rates for every year until 2050.[2] Although Mn production is greater than Ni and Co production, limited refining capacity for 'battery-grade' Mn forecasts supply shortages by 2030.[3,4] Even with $LiFePO_4$ (LFP), refinement bottlenecks for battery-grade P imply supply shortages by 2030.[5] Cathodes reliant only on industrial metals, or industrial elements, would alleviate the supply challenges that impede the 'net zero by 2050' goal. We classify 'industrial elements' as elements with global production of at least 10^7 metric tons in 2023 in primarily elemental form with $\gtrapprox$90 wt% purity. For example, Al, Fe, and S all meet these criteria, while Ni, Co, Mn, and P do not.[6,7] While Li itself does not meet the criteria, 'beyond Li-ion' batteries (e.g., Na-ion, aqueous Zn-ion, etc.) without any Li re-

quire new infrastructure, time, and investment to reach scale.[4,8,9] By contrast, next-generation Li-ion battery cathodes that contain only industrial elements, except for Li, could scale faster and at lower capital expenditure (CapEx) into Li-ion batteries by using existing infrastructure, just as Si anodes have already entered the market.[4]

Fe is the most globally produced transition metal, motivating research to develop high-performance cathodes that leverage Fe redox. The resurgence of LFP in commercial applications stems from its lower cost and more industrial element-like composition compared to NMC,[10] despite LFP's low energy density (≈580 Wh·kg^{-1}, ≈2068 Wh·L^{-1})[11] compared to, for example, NMC811 (≈950 Wh·kg^{-1}, ≈4500 Wh·L^{-1}).[12] Just over a decade ago, efforts to develop Fe-based cathodes that outperform LFP sought to increase the voltage of $Fe^{2+/3+}$ redox. By means of iono-covalency/inductive effects, the voltage can be shifted by over ≈1.1 V[13] to a maximum of 3.9 V vs. Li/Li$^+$ in triplite $LiFeSO_4F$.[14] However, the energy density of $LiFeSO_4F$ remained close to that of LFP, limiting its commercial viability.[15] More recently, Heo et al. over-discharged amorphous $LiFeSO_4F$, achieving 906 Wh·kg^{-1}.[16] However, this required converting $LiFeSO_4F$ to Li_2O, Fe^0, and $LiSO_3F$, and also required Li$^+$ at the anode in the as-assembled cell – requirements incompatible with current manufacturing techniques. Overall, high voltage $Fe^{2+/3+}$ redox in Fe-based cathodes has been unable to match the energy density of NMC, and high energy density requires conversion reactions.

Multielectron transition metal and anion redox processes in Li-rich materials invoke both intercalation and bond-forming/breaking reactions,[17] surpassing capacity limits of traditional single-e$^-$ transition metal redox. However, stabilizing the delithiated, oxidized state remains a key challenge. Multielectron redox increases energy density by increasing capacity, requiring reversible redox reactions even at deep delithiation levels. Initial delithiation involves 'transition metal oxidation,' emptying associated covalent d-p states.[18,19] Deep delithiation, however, yields under-coordinated anions, creating associated nonbonding p states near the Fermi level.[18,20–23] Often, the empty d-p states lie below the filled nonbonding p states, triggering anion to metal charge transfers that, in oxides, create reactive O peroxides/superoxides and promote $O_{2(g)}$ release.[20,21,24–27] The electronic reorganization and structural changes hinder electrochemically mediated anion redox involving the nonbonding p states. This issue is acute in Li-rich Fe-based oxides, specifically $Li_{1.17}Ti_{0.33}Fe_{0.5}O_2$[21] and $Li_{1.33}Fe_{0.33}Sb_{0.33}O_2$,[24] where deep delithiation incurs charge transfers from O^{2-} to $Fe^{3+/4+}$, associated with large hysteresis (≈1.4 V) and capacity fade (≈20% per cycle).

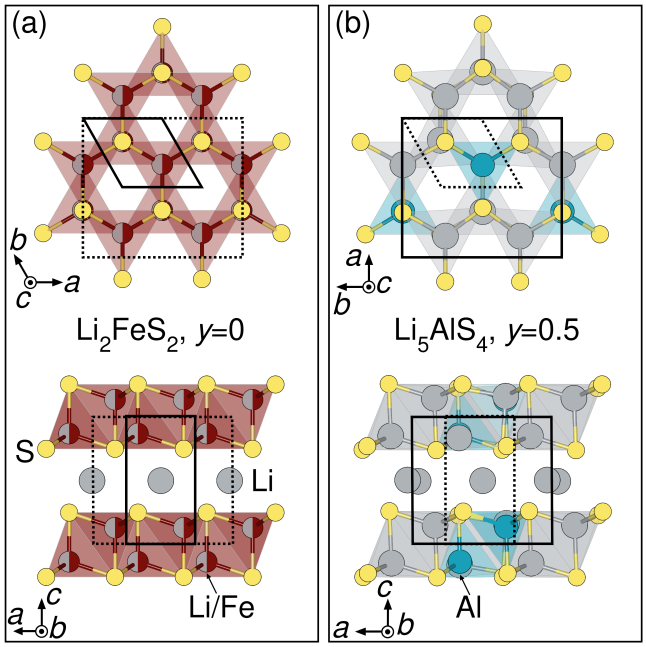

Figure 1: The crystal structure of (a) Li_2FeS_2 projected along the c-axis (top) and b-axis (bottom), and the crystal structure of (b) Li_5AlS_4 projected along the c-axis (top) and b-axis (bottom). In each panel, the solid black line indicates the unit cell of the structure shown, while the dashed black line indicates the unit cell of the other structure for comparison.

Here, to develop a Li-ion battery cathode entirely composed of industrial elements that achieves high energy density through multielectron redox, we target Li-rich, Fe-based sulfides derived from Li_2FeS_2. Sulfides must have extremely high capacities and thus high Li content to match the energy density of NMC because S is heavier and less electronegative than O. For example, $Li_{1.13}Ti_{0.57}Fe_{0.3}S_2$ achieves only up to ≈600 Wh·kg^{-1},[28] despite having greater capacity in mole e$^-$ per f.u. than NMC cathodes. The crystal structure of Li_2FeS_2,[29] shown in Figure 1a along the c and b axes, adopts the P$\bar{3}$m1 trigonal space group with a hexagonal close-packed (HCP) sulfide anion framework and cations alternating between octahedral and tetrahedral sites in lay-

ers. Occupation of tetrahedral sites in the HCP sulfide anion framework enables higher Li content and thus higher capacity than typical Li-rich materials, which feature FCC anion frameworks and solely octahedral cation sites. Li_2FeS_2, studied for decades (see Supplementary Note S1), exhibits multielectron redox during charge by $Fe^{2+/3+}$ oxidation of Fe-S $3d$-$3p$ states, followed by $2\,S^{2-}/(S_2)^{2-}$ oxidation[30] of S $3p$ nonbonding states.[22] Inspired by the structural similarities between Li_2FeS_2 and the more Li-rich Li_5AlS_4, shown in Figure 1 and discussed in Structural characterization of $Li_{2+y}Al_yFe_{1-2y}S_2$ (vide infra), we control Fe and S contributions to multielectron redox by substituting Li^+ and Al^{3+} for $2\,Fe^{2+}$ to yield $Li_{2+y}Al_yFe_{1-2y}S_2$ ($0\leq y \leq 0.5$). Al is the second most industrial metal after Fe[6] and is relatively light. S is an abundant byproduct of processing fossil fuels[6] and exists as stable persulfides $(S_2)^{2-}$ in many $3d$ transition metal sulfides.[17] Together, Fe, Al, and S are highly attractive from scalability and performance perspectives. We demonstrate that $Li_{2.2}Al_{0.2}Fe_{0.6}S_2$ achieves high gravimetric capacity ($\gtrapprox$450 mAh·g^{-1}) and energy density ($\gtrapprox$1000 Wh·kg^{-1}) through extensive redox of ≈75% of the S, with much less capacity fade (≈1.8% per cycle) than Li-rich Fe-based oxides (≈20% per cycle).[21,24] We compare multielectron redox in Li_2FeS_2 and $Li_{2.2}Al_{0.2}Fe_{0.6}S_2$ to understand why the latter accesses more S redox. We find that Al^{3+} stabilizes the delithiated state, suppressing internal charge transfers and structural changes, enabling electrochemically mediated anion redox over a wider capacity window. This insight creates new opportunities for developing next-generation Li-ion battery cathodes composed of scalable, industrial elements towards widespread deployment of Li-ion batteries to meet the 'net zero by 2050' goal.

Main

Structural characterization of $Li_{2+y}Al_yFe_{1-2y}S_2$

Substitution of Al^{3+} into Li_2FeS_2 is motivated by its structural similarity to Li_5AlS_4. Lim et al. first reported Li_5AlS_4 in 2018 and noted its structural similarity to Li_2FeS_2,[31] which others soon reiterated.[32–34] The crystal structure of Li_5AlS_4,[31] shown in Figure 1b along the c and b axes, adopts the $P2_1/m$ monoclinic space group with a unit cell that is a supercell of the primitive unit cell in $P\bar{3}m1$ if β were allowed to deviate slightly to equal 90° from 90.333°. The primary difference between Li_2FeS_2 and Li_5AlS_4 lies in the tetrahedral cation site occupancy. Li_2FeS_2 has disordered Li/Fe at a 1:1 ratio (Figure 1a), while Li_5AlS_4 has ordered Li/Al at a 3:1 ratio (Figure 1b). The ordering in Li_5AlS_4 slightly distorts its anion framework, yet we anticipate that yLi^+ and yAl^{3+} can be substituted for $2yFe^{2+}$ in Li_2FeS_2, to yield $Li_{2+y}Al_yFe_{1-2y}S_2$ ($0\leq y \leq 0.5$).

We synthesize Li_2FeS_2 (y=0), $Li_{2.2}Al_{0.2}Fe_{0.6}S_2$ (y=0.2), and $Li_{2.4}Al_{0.4}Fe_{0.2}S_2$ (y=0.4) by solid-state synthesis from Li_2S, FeS, and Al_2S_3 at 900 °C. To confirm the substitution, we analyze synchrotron X-ray diffraction (sXRD) patterns for Li_2FeS_2, $Li_{2.2}Al_{0.2}Fe_{0.6}S_2$, and $Li_{2.4}Al_{0.4}Fe_{0.2}S_2$ shown in Figure 2a, b, and c, respectively, with the corresponding Rietveld refinements, reflections associated with each phase in the fit, and the difference between the fit and data. We use the larger $P2_1/m$ unit cell to fit all materials, comparing their lattice parameters. Site occupancy is determined by a linear combination of the two end-members, weighted according to the target stoichiometry. We detect 5.9 wt% FeS[35] in Li_2FeS_2, but fit both $Li_{2.2}Al_{0.2}Fe_{0.6}S_2$ and $Li_{2.4}Al_{0.4}Fe_{0.2}S_2$ to single phases. The lattice parameters a, b, and c from the fits, plotted vs. Al content in Figure 2d, e, and f, respectively, follow linear Vegard trends, confirming the substitution. The refined phases deviate more from HCP symmetry as y increases (Figure S1), corroborating the Vegard trend. We also verify the stoichiometries of Li_2FeS_2 and $Li_{2.2}Al_{0.2}Fe_{0.6}S_2$ by inductively coupled plasma mass spectrometry (ICP-MS) and combustion analysis (Table S1). We mark certain unfit reflections between 1 to 2 Å^{-1} for Li_2FeS_2 and $Li_{2.2}Al_{0.2}Fe_{0.6}S_2$ with asterisks (*), identifying them as likely superstructure reflections after ruling out several possible impurities (see Table S2) and considering historical discrepancies regarding superstructure in Li_2FeS_2 (see Supplementary Note S2).

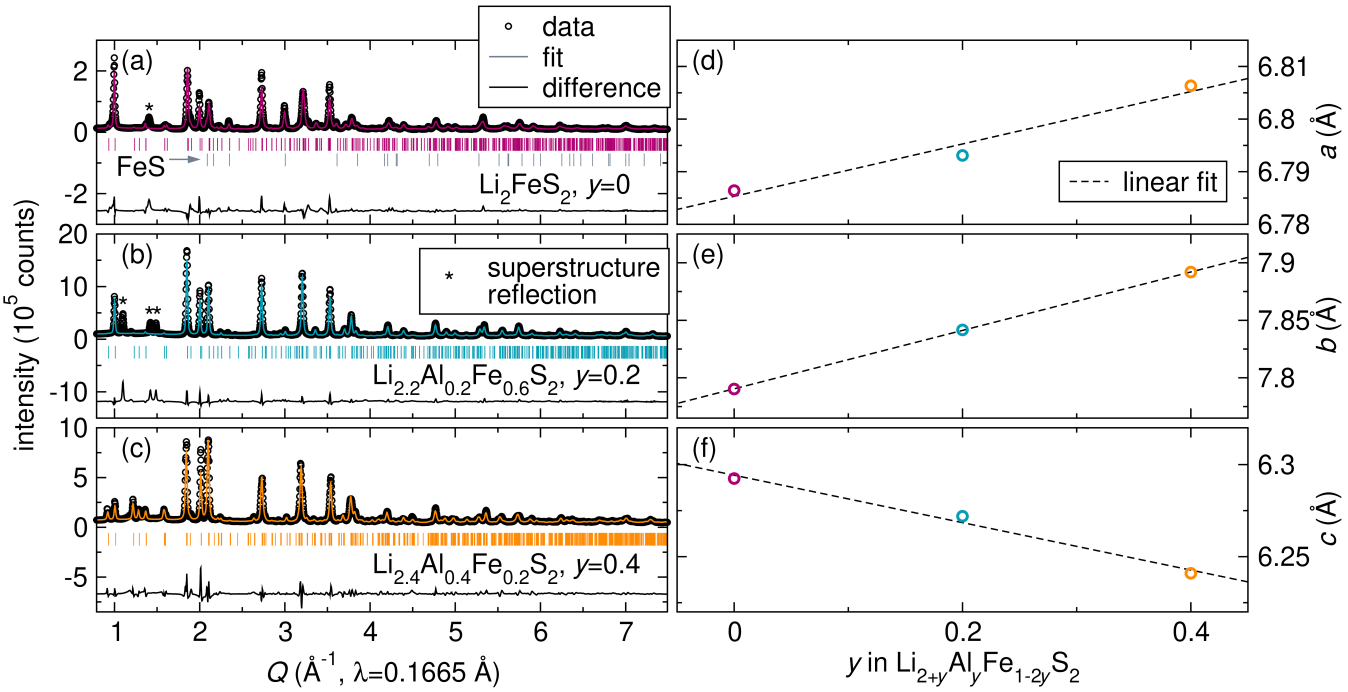

Figure 2: Synchrotron powder X-ray diffraction of (a) Li_2FeS_2, (b) $Li_{2.2}Al_{0.2}Fe_{0.6}S_2$, and (c) $Li_{2.4}Al_{0.4}Fe_{0.2}S_2$. The corresponding Rietveld refinement, reflection locations in Q (Å^{-1}) of each phase in the fit, and difference between fit and data are shown for each material. Superstructure reflections that are not fit by the Rietveld refinement are indicated by asterisks (*). The resulting lattice parameters (d) a, (e) b, and (f) c from each Rietveld refinement with respect to y in $Li_{2+y}Al_yFe_{1-2y}S_2$ with linear fits indicated by dashed lines. The lattice parameters follow a linear Vegard's trend, indicating that yLi$^+$ and yAl^{3+} successfully substitute for $2y$Fe^{2+} in $Li_{2.2}Al_{0.2}Fe_{0.6}S_2$ ($y = 0.2$) and $Li_{2.4}Al_{0.4}Fe_{0.2}S_2$ ($y = 0.4$).

Electrochemical characterization of $Li_{2+y}Al_yFe_{1-2y}S_2$

The electrochemical performance is evaluated with galvanostatic cycling. The first cycles of Li_2FeS_2, $Li_{2.2}Al_{0.2}Fe_{0.6}S_2$, and $Li_{2.4}Al_{0.4}Fe_{0.2}S_2$ at C/10 based on 1 e$^-$ per formula unit are shown in Figure 3a, b, and c, respectively. All materials exhibit the sloping Fe$^{2+/3+}$ oxidation region followed by the $2\,S^{2-}/(S_2)^{2-}$ plateau during charge.[30] A dashed line across Figure 3a, b, and c indicates a linear decrease in Fe oxidation capacity with y, confirming its proportionality to Fe content. We find that ≈60% to 75% of the Fe is oxidized during charge, suggesting an oxidation state limit between Fe$^{\approx 2.60+}$ to Fe$^{\approx 2.75+}$. The S oxidation capacity is greater for $Li_{2.2}Al_{0.2}Fe_{0.6}S_2$ (1.52 ±0.09 e$^-$) than Li_2FeS_2 (1.09 ±0.01 e$^-$), but does not increase much further for $Li_{2.4}Al_{0.4}Fe_{0.2}S_2$ (1.63 ±0.21 e$^-$). Three replicate cells from separate reaction batches for each material are shown in Figure S2, with tabulated capacities provided in Table S3.

We use the galvanostatic intermittent titration technique (GITT) to assess how kinetic properties change with y. The equilibrium voltage and overpotential during charge for Li_2FeS_2, $Li_{2.2}Al_{0.2}Fe_{0.6}S_2$, and $Li_{2.4}Al_{0.4}Fe_{0.2}S_2$, extracted from GITT, are shown in Figure 3d and e. Full GITT charge/discharge curves and representative relaxation curves are shown in Figure S3. $Li_{2.4}Al_{0.4}Fe_{0.2}S_2$ exhibits higher S oxidation overpotentials than Li_2FeS_2 and $Li_{2.2}Al_{0.2}Fe_{0.6}S_2$, which have identical overpotentials despite different Al^{3+} contents. The high Al^{3+} content of 0.4 heavily distorts the anion framework (Figure S1), likely hindering structural distortions required for facile S redox.

Due to the low capacity, large hysteresis, and sluggish kinetics in $Li_{2.4}Al_{0.4}Fe_{0.2}S_2$, we now focus on Li_2FeS_2 and $Li_{2.2}Al_{0.2}Fe_{0.6}S_2$. We show the capacity fade of Li_2FeS_2 and $Li_{2.2}Al_{0.2}Fe_{0.6}S_2$ at C/10 over 25 cycles in Figure 3f. Each data point and error bar represent the average and standard deviation of three replicate cells (Figure S4 shows individual cell data). We find that the capacity of Li_2FeS_2 fades more slowly, at ≈0.64% per cycle, compared to $Li_{2.2}Al_{0.2}Fe_{0.6}S_2$, which fades at ≈1.76% per cycle. Despite the fade, the galvanostatic curves of both materials retain their shape over multiple cycles (see Figure S5). The greater capacity fade of $Li_{2.2}Al_{0.2}Fe_{0.6}S_2$ is

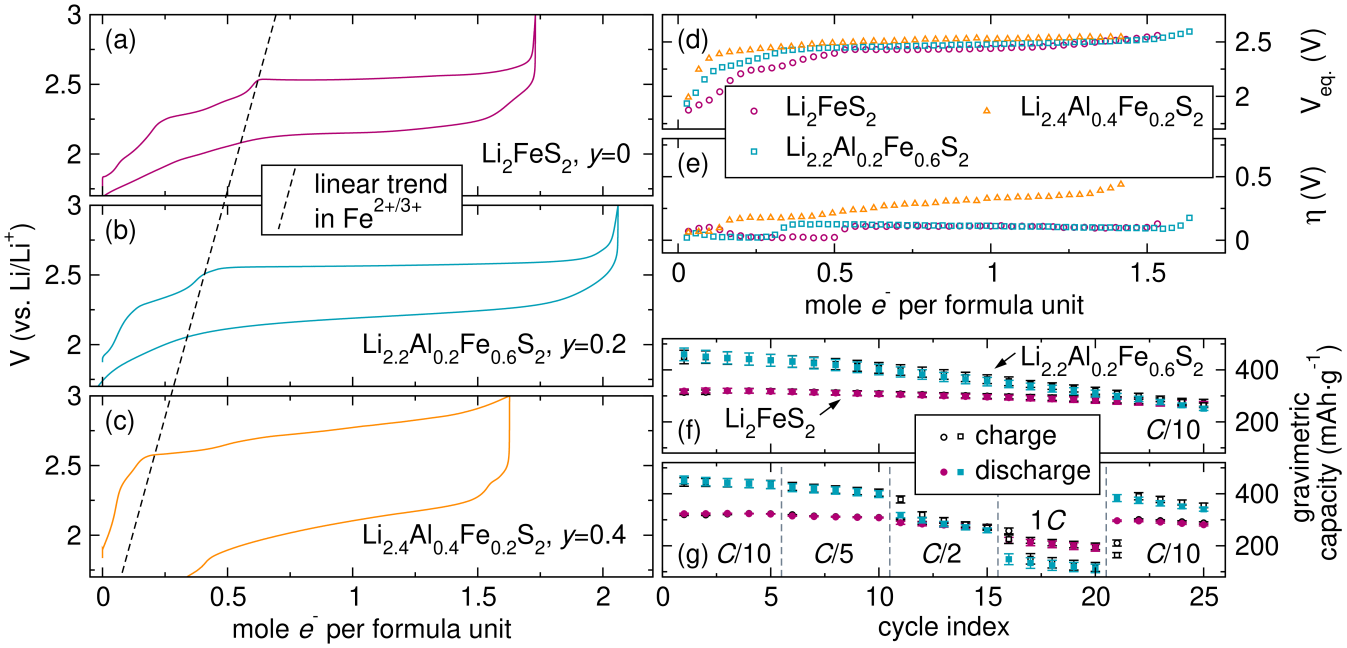

Figure 3: First cycle galvanostatic charge and discharge curves of (a) Li_2FeS_2, (b) $Li_{2.2}Al_{0.2}Fe_{0.6}S_2$, and (c) $Li_{2.4}Al_{0.4}Fe_{0.2}S_2$ cycled at $C/10$ based on 1 e^- per formula unit. The dashed line across panels (a), (b), and (c) indicates the linear trend in Fe oxidation capacity with y. (d) The equilibrium voltage $V_{eq.}$ and (e) overpotential η during the first charge extracted from GITT. (f) The cycling of Li_2FeS_2 and $Li_{2.2}Al_{0.2}Fe_{0.6}S_2$ at $C/10$. (g) Rate capability tests of Li_2FeS_2 and $Li_{2.2}Al_{0.2}Fe_{0.6}S_2$ for 5 cycles each at $C/10$, $C/5$, $C/2$, 1C, and again at $C/10$. All C rates are based on 1 e^- per formula unit. The data points in (f) and (g) are the average of three replicate cells and error bars indicate the standard deviations.

unsurprising, given that 76.9±1.5% of the total capacity comes from S redox, which incurs structural distortions, relative to only ≈65±1.5% in Li_2FeS_2 (Table S3). We also compare the rate capabilities of Li_2FeS_2 and $Li_{2.2}Al_{0.2}Fe_{0.6}S_2$ in Figure 3g (Figure S6 shows individual cell data). While Li_2FeS_2 retains more capacity at $1C$ compared to $Li_{2.2}Al_{0.2}Fe_{0.6}S_2$, both exhibit larger hysteresis at $1C$ (see Figure S7), and $Li_{2.2}Al_{0.2}Fe_{0.6}S_2$ retains its greater capacity upon returning to $C/10$. We note, however, that we use free standing electrodes (see Freestanding cathode preparation), which are poorly suited for extended cycling. We are optimizing cast electrodes to better assess the capacity fade and rate capability. Regardless, $Li_{2.2}Al_{0.2}Fe_{0.6}S_2$ achieves extremely high initial charge/discharge capacities of 449±20 mAh·g^{-1}/446±24 mAh·g^{-1} and energy densities of 1125±49/1024±55 Wh·kg^{-1} (see Table S4 for the gravimetric capacities, average voltages, and energy densities of Li_2FeS_2 and $Li_{2.2}Al_{0.2}Fe_{0.6}S_2$).

Spectroscopic characterization of the multielectron redox mechanism

We spectroscopically characterize Li_2FeS_2 and $Li_{2.2}Al_{0.2}Fe_{0.6}S_2$ to evaluate charge compensation and check assignments of features in the galvanostatic data. We measure *ex-situ* Fe and S K-edge X-ray absorption spectroscopy (XAS) at six states of charge (SOCs) for both materials: (1) pristine, (2) mid-slope (halfway through the sloping region), (3) transition (at the transition point between the sloping and plateau regions), (4) mid-plateau (halfway through the plateau region), (5) charged, and (6) discharged.

First, we discuss the Fe K-edge XAS in Figure 4. The Fe K-edge near-edge regions for Li_2FeS_2 and $Li_{2.2}Al_{0.2}Fe_{0.6}S_2$ at the various SOCs are shown in Figure 4a and b. The spectra exhibit common features: a pre-edge at ≈7113.0 eV (labeled x), and a rising edge at ≈7117.2 eV (y) or ≈7118.2 eV (z), depending on the SOC. For both materials, the pre-edge intensity increases at the transition SOC and stays constant at the charged state, suggesting that S oxidation does not affect Fe-S covalency or the Fe coordination environment.[36] The maxima of the first derivatives of the rising edge, shown in Figure 4c and d for Li_2FeS_2 and $Li_{2.2}Al_{0.2}Fe_{0.6}S_2$,

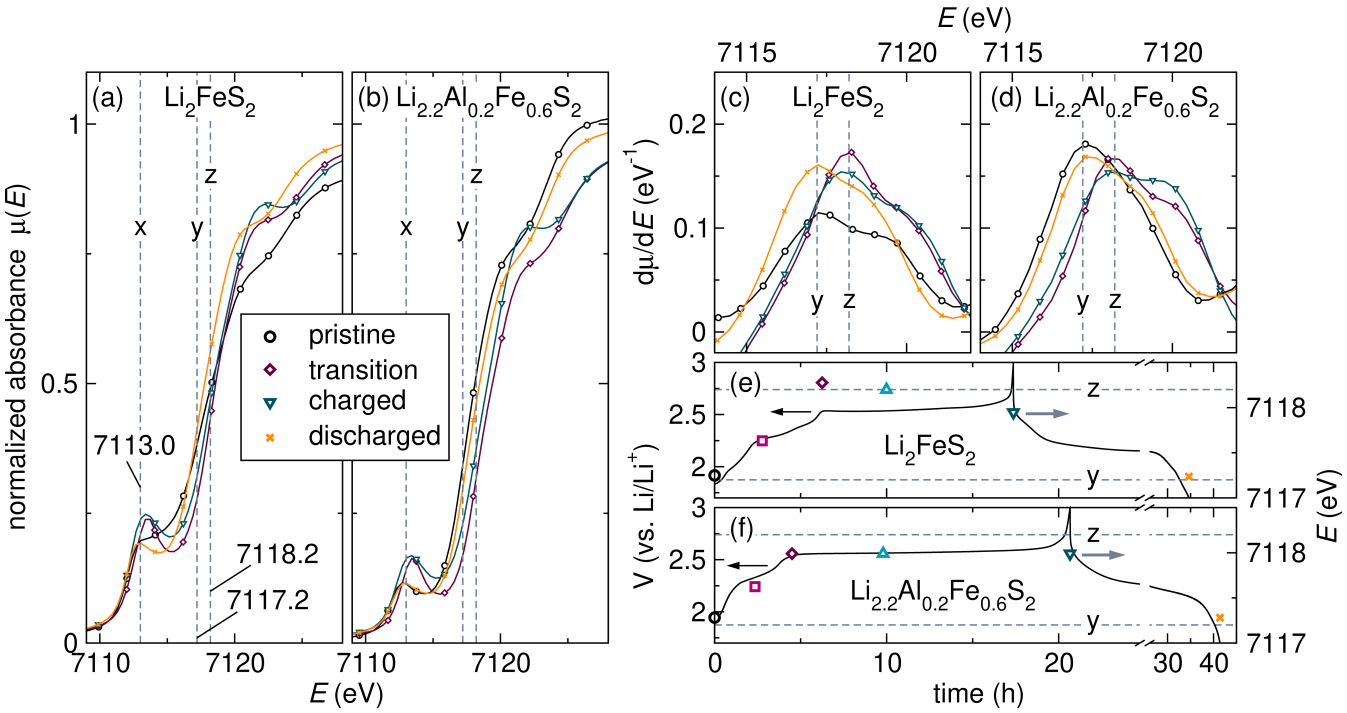

Figure 4: *Ex-situ* Fe K-edge XAS spectra of (a) Li_2FeS_2 and (b) $Li_{2.2}Al_{0.2}Fe_{0.6}S_2$. The first derivative of the rising edge regions for (c) Li_2FeS_2 and (d) $Li_{2.2}Al_{0.2}Fe_{0.6}S_2$. The energies of the maxima of the first derivatives at each of the SOCs are overlaid with the corresponding galvanostatic cycling data for (e) Li_2FeS_2 and (f) $Li_{2.2}Al_{0.2}Fe_{0.6}S_2$. The dashed lines in all panels indicate the approximate positions of the pre-edge x, at 7113.0 eV, and the two rising edges observed at different SOCs, y and z, at 7117.2 eV and 7118.2 eV, respectively. The data for the pristine, transition, charged, and discharged states of Li_2FeS_2 are adapted with permission from Hansen et al.[30] Copyright 2020 American Chemical Society.

increase by ≈1 eV from ≈7117.2 eV in the pristine state to ≈7118.2 eV at the transition SOC, and stay constant at the charged state. This confirms that Fe oxidation ceases after the transition SOC despite the majority of electron removal occurring during the plateau. The data from intermediate mid-slope and mid-plateau SOCs, shown in Figure S8, further support this finding. We summarize this result in Figure 4e,f, overlaying the rising edge positions with the galvanostatic data. For both Li_2FeS_2 and $Li_{2.2}Al_{0.2}Fe_{0.6}S_2$, the rising edge position increases during the sloping region indicating oxidation, and stays constant during the plateau.

Next, we discuss the S K-edge XAS in Figure 5. The Li_2FeS_2 spectra and corresponding galvanostatic data, shown in Figure 5a and b, is reproduced from Hansen et al.[30] with two new data points at the mid-slope and mid-plateau SOCs. During the sloping region, the pre-edge feature labeled v at 2469.2 eV grows in intensity, indicating greater Fe-S covalency.[30,37] During the plateau, a new pre-edge feature labeled w at 2471.8 eV emerges that indicates persulfide formation,[30] peaking in intensity at the charged state and vanishing at the discharged state. The appearance of the pre-edge feature w marks a switch from increasing Fe-S covalency to forming S-S bonds. The $Li_{2.2}Al_{0.2}Fe_{0.6}S_2$ spectra and corresponding galvanostatic data in Figure 5c and d exhibit the same trends as Li_2FeS_2, with pre-edge features v and w labeled at the same energies. The greater S oxidation capacity of $Li_{2.2}Al_{0.2}Fe_{0.6}S_2$ is confirmed by the much greater intensity of the pre-edge feature w at the charged state. The S oxidation is structurally reversible in both materials, as confirmed by *ex-situ* XRD (Supplementary Note S4 and Figures S9 and S10).

Stability of $Li_{2-x}FeS_2$ and $Li_{2.2-x}Al_{0.2}Fe_{0.6}S_2$

While the Fe and S K-edge XAS confirm greater S redox capacity in $Li_{2.2}Al_{0.2}Fe_{0.6}S_2$ than in Li_2FeS_2, the critical question of *why* remains unanswered. We rule out the higher Li^+ content of $Li_{2.2}Al_{0.2}Fe_{0.6}S_2$ as the reason, since $Li_{2.4}Al_{0.4}Fe_{0.2}S_2$ has even more Li^+ but no greater S redox capacity. Moreover, this reasoning would imply a higher total cation content in the charged state for $Li_{2.2}Al_{0.2}Fe_{0.6}S_2$ than Li_2FeS_2, which

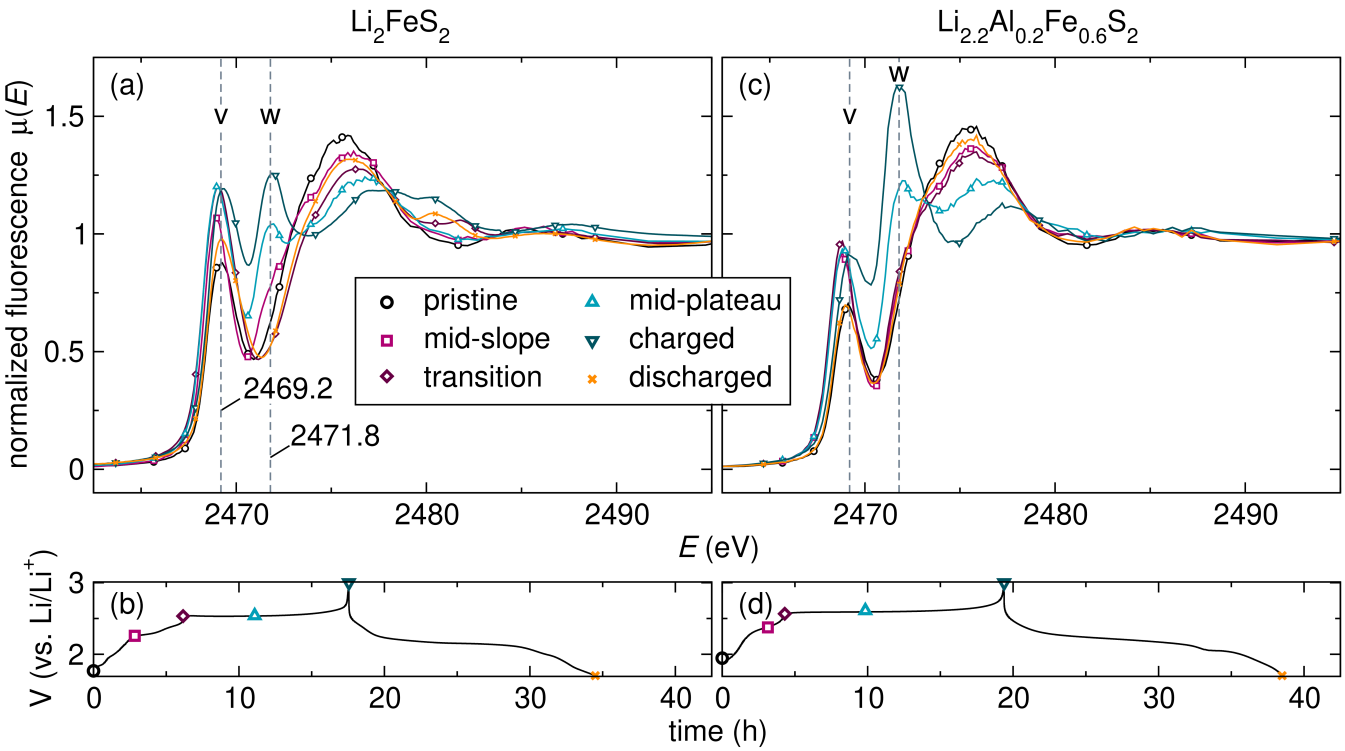

Figure 5: (a) *Ex-situ* S K-edge XAS and (b) a representative first cycle curve indicating the SOCs at which the XAS data was collected for Li_2FeS_2. The corresponding data for $Li_{2.2}Al_{0.2}Fe_{0.6}S_2$ are in (c) and (d), respectively. The dashed lines in (a) and (c) indicate the two pre-edge features v and w, at 2469.2 eV and 2471.8 eV, respectively. The data for the transition, charged, and discharged SOCs of Li_2FeS_2 are adapted with permission from Hansen et al.[30] Copyright 2020 American Chemical Society.

is not the case (see Supplementary Note S5). As discussed in the Introduction, a key challenge in developing cathodes that access anion redox is stabilizing the delithiated, oxidized state. When evaluating the capacity limits of multi-electron redox cathodes, considering the most thermodynamically stable structure of the fully oxidized/delithiated material offers insights into the relative stability of the electrochemically oxidized/delithiated state. Fully delithiated Li_2FeS_2 would yield FeS_2, with the thermodynamically stable pyrite structure that features octahedral Fe^{2+} and all $(S_2)^{2-}$. Thus, we hypothesize that as deep delithiation approaches the FeS_2 stoichiometry, electrochemically oxidized $Fe^{2+/3+}$ becomes unstable alongside remaining S^{2-} compared to Fe^{2+} and $(S_2)^{2-}$. However, the phase transition to FeS_2 requires major structural changes, kinetically trapping the electrochemically oxidized material. As more persulfides form during charge, the stoichiometry and overall oxidation states approach pyrite FeS_2, and we hypothesize that the kinetic stabilization eventually fails, causing the voltage to polarize before full delithiation.

We now consider the thermodynamically stable structure of fully delithiated $Li_{2.2}Al_{0.2}Fe_{0.6}S_2$, i.e., '$Al_{0.2}Fe_{0.6}S_2$'. There is no reported Al-Fe-S ternary material with the composition $Al_{0.2}Fe_{0.6}S_2$ (i.e., '$AlFe_3S_{10}$'). Thus, to determine the thermodynamically stable configuration of $Al_{0.2}Fe_{0.6}S_2$, we attempt the solid state reaction of Al, Fe, and S in the stoichiometric ratio of $Al_{0.2}Fe_{0.6}S_2$ at 900 °C. We quantify the phases in the reaction product by XRD and Rietveld analysis, shown in Figure S11. The pattern is well described by a fit to three separate phases: pyrite FeS_2[38] (51.1 wt%), 'Fe-deficient' FeS Fe_7S_8[39] (10.6 wt%), and the Al-Fe-S ternary Al_2FeS_4[40–42] (38.3 wt%). Although the majority phase is still FeS_2, the formation of Al_2FeS_4 shows that the thermodynamic state of fully delithiated $Li_{2.2}Al_{0.2}Fe_{0.6}S_2$ includes an Al-Fe-S ternary, rather than separate Fe-S and Al-S binaries. Importantly, Al_2FeS_4 crystallizes in the $P\bar{3}m1$ trigonal space group with an HCP sulfide anion framework and cations in octahedral edge-sharing and tetrahedral corner-sharing sites,[40–42] similar to $Li_{2+y}Al_yFe_{1-2y}S_2$ materials with HCP-like anion frameworks and analogous cation sites (Figure S12). Thus, a thermodynamically stable fully delithiated ternary phase exists, requir-

ing far less structural reorganization than converting to pyrite. We hypothesize that this stabilizes $Fe^{2+/3+}$ alongside S^{2-}, suppressing the phase transition to FeS_2 and enabling greater anion oxidation in $Li_{2.2}Al_{0.2}Fe_{0.6}S_2$.

To assess the relative thermodynamic and kinetic stabilities of delithiated $Li_{2-x}FeS_2$ and $Li_{2.2-x}Al_{0.2}Fe_{0.6}S_2$, we conduct annealing and resting experiments. For both experiments, we charge the cathode to the transition SOC, stop the cell, remove and rinse the cathode, then either anneal it in an evacuated ampule (≈50 mTorr) at 200 °C for 2 hours or rest it at room temperature under the same static vacuum for ≈1 week, and finally reassemble a new cell with the annealed or rested cathode. At the transition point, 'exposed' S $3p$ nonbonding states would have been oxidized if charging had continued. Thus, annealing/resting at the transition SOC reveals the thermodynamic/kinetic stability of these exposed S $3p$ nonbonding states relative to empty Fe-S $3d$-$3p$ states (or vice versa).

The galvanostatic data from the annealing and resting experiments, along with XRD and S K-edge XAS are shown in Figure 6. The charge curves after annealing and resting Li_2FeS_2 charged to the transition point are shown in Figure 6a. After annealing, the OCV decreases by ≈0.32 V from the transition SOC, with new, distinct plateaus in the charge curve. After resting, the OCV decreases by ≈0.26 V, and the charge curve of the rested cathode shows a new Fe oxidation-like slope followed by a S oxidation plateau, suggesting $Fe^{2+/3+}$ can be reduced by S^{2-} even without heat. Combustion analysis (Table S5) shows S loss of ≈0.6 wt% after annealing, which is negligible and too low to explain the changes in the electrochemistry. To check for structural changes and FeS_2 formation after annealing, we compare *ex-situ* XRD of Li_2FeS_2 in the pristine, transition, and annealed states (Figure 6b). After annealing, we observe reduced (0 0 1) intensity for Li_2FeS_2, indicating lower crystallinity, and ≈17 wt% FeS_2 determined by Rietveld refinement (Figure S13a). The formation of FeS_2 is evident from its (2 0 0) reflection at ≈33.1 2θ. The FeS_2 formation shows that the S $3p$ nonbonding states are unstable relative to empty Fe-S $3d$-$3p$ states. We confirm the presence of $(S_2)^{2-}$ by S K-edge XAS of the annealed cathode, observing intensity at the previously noted pre-edge feature w (Figure 6c). Thus, electrochemically oxidized $Li_{2-x}FeS_2$ ($x \approx 0.58 \pm 0.05$) is a kinetically stabilized, metastable phase. During annealing, it loses crystallinity, converts to FeS_2, and forms persulfides. After resting at room temperature, Fe appears reduced but without incurring structural changes.

We now discuss the same experiments for $Li_{2.2}Al_{0.2}Fe_{0.6}S_2$. The charge curves after annealing and resting $Li_{2.2}Al_{0.2}Fe_{0.6}S_2$ charged to the transition point are shown in Figure 6d. After annealing, the OCV decreases by ≈0.26 V, a smaller decrease than in Li_2FeS_2, with the S oxidation plateau unaltered except for a small initial Fe oxidation-like feature. After resting, the OCV decreases by ≈0.23 V, almost matching the OCV after annealing, again with the S oxidation plateau unaltered and an even smaller initial Fe oxidation-like feature. This similarity suggests that the 200 °C relaxation process is an accelerated version of the room temperature process. Combustion analysis shows no S loss (Table S5). XRD (Figure 6e) shows that in the annealed state, unlike Li_2FeS_2, the (0 0 1) intensity increases, indicating higher crystallinity, with no impurities in the Rietveld refinement (Figure S13b). S K-edge XAS confirms the absence of persulfides in the annealed cathode, with no new intensity at the pre-edge feature w (Figure 6f). Although $Li_{2.2-x}Al_{0.2}Fe_{0.6}S_2$ ($x \approx 0.46 \pm 0.02$) is kinetically stabilized, conversion to FeS_2 is suppressed during annealing, with similar changes after both annealing and resting. Thus, the annealed and relaxed states of $Li_{2.2-x}Al_{0.2}Fe_{0.6}S_2$ ($x \approx 0.46 \pm 0.02$) are much more similar than in $Li_{2-x}FeS_2$ ($x \approx 0.58 \pm 0.05$).

Electronic and local structure of Fe in $Li_{2-x}FeS_2$ and $Li_{2.2-x}Al_{0.2}Fe_{0.6}S_2$

The annealing experiments strongly suggest that the instability of the delithiated materials is associated with empty Fe-S $3d$-$3p$ states. Li_2FeS_2 undergoes formal charge transfer from S^{2-} to $Fe^{\gtrsim 2.6+}$, yielding Fe^{2+} and $(S_2)^{2-}$ in FeS_2, while $Li_{2.2}Al_{0.2}Fe_{0.6}S_2$ shows an Fe oxidation-like voltage response, suggesting Fe is reduced during annealing and re-oxidized during charge. Fe K-edge XAS confirms formal Fe reduction in both annealed materials (Supplementary Note S3 and Fig-

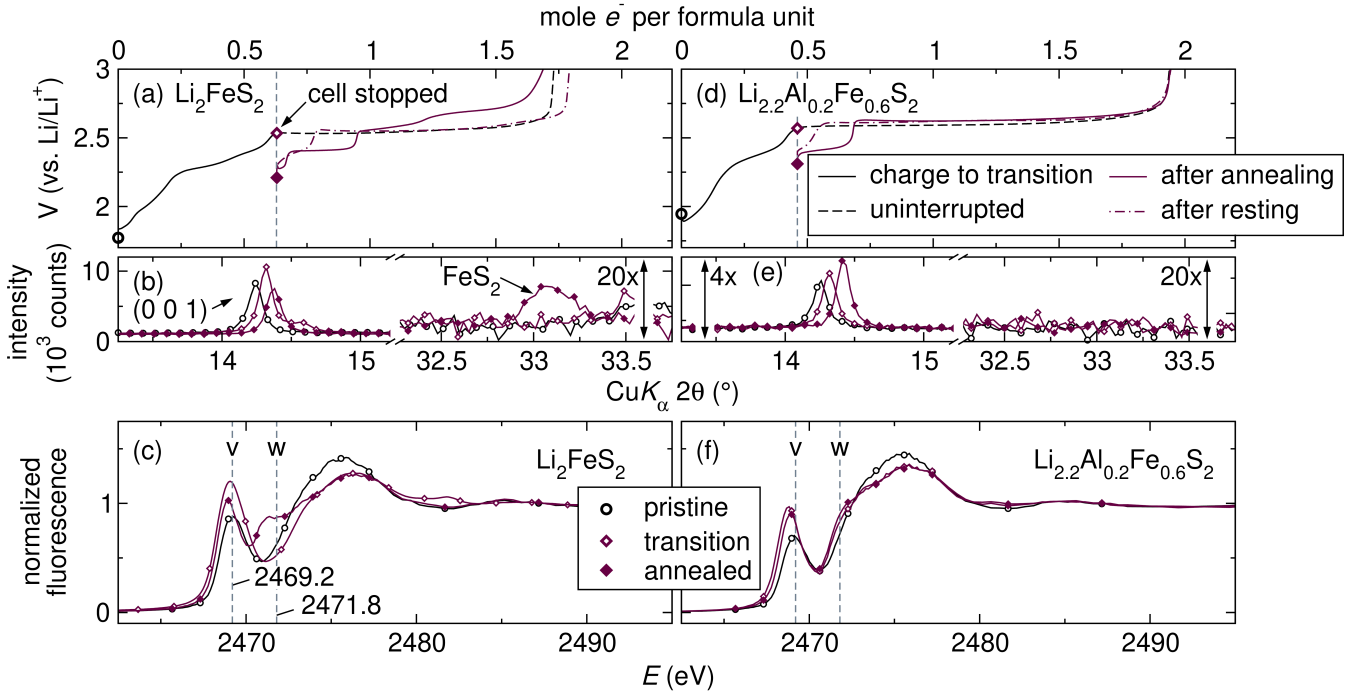

Figure 6: (a) Charge curves of Li_2FeS_2 up to the transition point, after which the cell is stopped, disassembled, the cathode is rinsed in DMC, dried in vacuum, annealed at 200 °C under static vacuum (≈50 mTorr) for 2 hours, or rested under the same vacuum conditions for ≈1 week, and then assembled in a new cell for galvanostatic cycling. The standard galvanostatic cycling charge curve for uninterrupted cycling is indicated by the black, dashed line in panel (a). (b) *Ex-situ* XRD of Li_2FeS_2 focused on the 2θ ranges for the (0 0 1) reflection, and the (2 0 0) reflection of pyrite FeS_2 in the pristine, transition, and annealed states. (c) S K-edge XAS spectra of Li_2FeS_2 in the pristine, transition, and annealed states. As before in Figure 5, the dashed lines in panel (c) indicate the two pre-edge features v and w, at 2469.2 eV and 2471.8 eV, respectively. Panels (d), (e), and (f), respectively, indicate the same corresponding data for $Li_{2.2}Al_{0.2}Fe_{0.6}S_2$. The data for the S K-edge XAS spectrum of Li_2FeS_2 at the transition point in (c) is adapted with permission from Hansen et al.[30] Copyright 2020 American Chemical Society.

ure S8). For $Li_{2.2}Al_{0.2}Fe_{0.6}S_2$, this raises the question of the electron source for Fe reduction since persulfide formation is not observed. We suggest that the charge compensation is similar to that in Fe-deficient Fe_7S_8 relative to FeS, where it's unclear whether the extra positive charge in Fe_7S_8 is Fe-based ($Fe_2^{3+}Fe_5^{2+}S_8^{2-}$),[43] S-based ($Fe_7^{2+}S_6^{2-}S_2^{-}$),[44] or some combination of both.[45,46]

We use Mössbauer spectrometry and Fe K-edge extended X-ray absorption fine structure (EXAFS) analysis, which are sensitive probes of the electronic and local structure of Fe, to evaluate the stability of Li_2FeS_2 and $Li_{2.2}Al_{0.2}Fe_{0.6}S_2$ at all SOCs, including materials annealed after charging to the transition point. In Figure 7, the Mössbauer isomer shift, reflecting Fe $3d$ state occupancy, and the first shell coordination number N from Fe K-edge EXAFS, representing the average number of nearest S atoms coordinating Fe, are plotted because they show the greatest differences between Li_2FeS_2 and $Li_{2.2}Al_{0.2}Fe_{0.6}S_2$, elucidating the role of Al^{3+}. The Mössbauer isomer shifts and quadrupole splittings can be found in Figure S14, with each fitted spectrum in Figures S15 and S16, and all fit parameters in Table S6. Each Mössbauer spectrum is fit with four distinct Fe sites, and the weighted average isomer shift and its weighted standard deviation for each spectrum are plotted in Figure 7a,d. A larger weighted standard deviation in the isomer shift reflects a wider spread among the four Fe sites used to fit each spectrum. The EXAFS first and second shell $r_{\text{eff.}}$ and N are shown in Figure S17, with the fitted $\chi(k)$ and $|\chi(R)|$ in Figures S18 and S19 and Figures S20 and S21, respectively, and all fit parameters in Table S7.

First, we discuss the Li_2FeS_2 isomer shifts and N in Figure 7a and b, with corresponding galvanostatic data (Figure 7c). The weighted average isomer shift decreases during the sloping region, which is consistent with Fe oxidation, and increases during discharge, consistent with Fe reduction. However, the average isomer shift unexpectedly increases during the S oxidation plateau, which is highlighted by the dotted/dashed line marking the average isomer shift at the transition point. The increase, confirmed by the spectral cen-

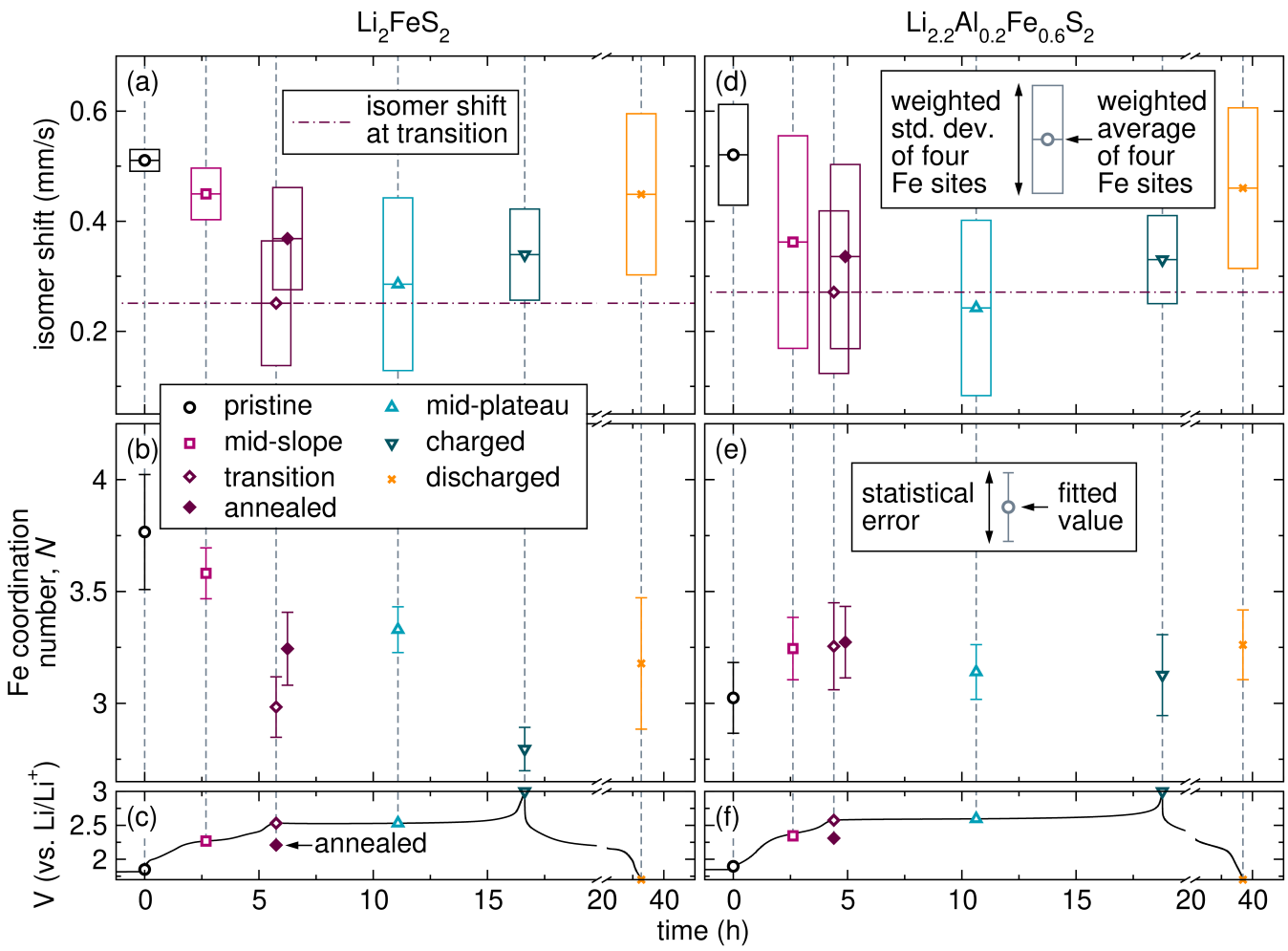

Figure 7: (a) The weighted averages and corresponding weighted standard deviations of the isomer shifts of the four Lorentzian doublets used to fit *ex-situ* Mössbauer spectra of Li_2FeS_2 at various SOCs. (b) The coordination number N of the first shell correlations, representing the average number of nearest S atoms coordinating Fe, extracted from EXAFS fits for Li_2FeS_2 at various SOCs. (c) The representative galvanostatic data showing the SOC for each data point. Panels (d), (e), and (f) indicate the same corresponding data, respectively, for $Li_{2.2}Al_{0.2}Fe_{0.6}S_2$. In panels (a) and (d), the weighted average is indicated by the symbol, and the weighted standard deviation is indicated by height of the box accompanying the symbol. The dotted/dashed dark purple horizontal line in panels (a) and (d) indicates the weighted average isomer shift at the transition SOC. The EXAFS data for the pristine, transition, charged, and discharged SOCs of Li_2FeS_2 are adapted with permission from Hansen et al.[30] Copyright 2020 American Chemical Society.

troids (Figure S22a,b), indicates a counterintuitive global Fe 'reduction' despite the $\approx 1.09 \pm 0.01$ e^- oxidation. A Mössbauer study in 1987 also observed this increase but did not explain it.[47] Covalency differences between $(S_2)^{2-}$ and S^{2-} cannot explain the increase, as $(S_2)^{2-}$, being more covalent (see Supplementary Note S6), would decrease, not increase, the isomer shift. Fe^{3+} reduction can occur when S^{2-} is present, even without formal $2\,S^{2-}/(S_2)^{2-}$ oxidation, as shown by the annealing experiment with $Li_{2.2}Al_{0.2}Fe_{0.6}S_2$, and suggested by the resting experiments with both materials. Thus, we deduce that the increase indicates genuine Fe^{3+} reduction in the *ex-situ* samples, which Mössbauer spectrometry is sensitive enough to detect.[48–50] Simultaneously, N decreases during charge, with $N \lessapprox 3$ indicating Fe distorts towards the basal face of the FeS_4 tetrahedron in the charged state, before tending towards the pristine state in the discharged state. The data in the annealed state are shown, but conclusions are avoided due to convolution from FeS_2. The samples are measured *ex-situ* ≈24 hours after cell disassembly and thus have time to relax, and so effectively represent the "rested" state discussed previously. Thus, the Fe reduction and distortion towards the FeS_4 tetrahedron basal face together characterize the kinetic relaxation mechanism at deep delithiation levels. The greater relaxation – that is, increasingly reduced and distorted Fe – with deeper delithiation, shows that empty Fe-S $3d$-$3p$ states indeed become increasingly unstable.

Next, we discuss the $Li_{2.2}Al_{0.2}Fe_{0.6}S_2$ isomer shifts and N in Figure 7d and e, with corresponding galvanostatic data (Figure 7f). The isomer shift largely mirrors Li_2FeS_2, with a notable difference at the mid-plateau SOC. Instead of the continuous increase during the S oxidation plateau observed for Li_2FeS_2, the isomer shift decreases slightly at the mid-plateau before increasing again at the charged state. This non-monotonicity, confirmed by the spectral centroids (Figure S22c,d), is highlighted by the dotted/dashed line once again marking the average isomer shift at the transition point. In Li_2FeS_2, the continuous increase reveals that empty Fe-S $3d$-$3p$ states grow more unstable with delithiation. Conversely, the decrease at the mid-plateau in $Li_{2.2}Al_{0.2}Fe_{0.6}S_2$ reveals that the empty states have slightly greater stability at this SOC than in Li_2FeS_2. Correspondingly, N stays mostly constant, with Fe near the base at all SOCs, even in the annealed state. The similarity of N in the annealed and transition states extends the previously observed similarity of these states in $Li_{2.2}Al_{0.2}Fe_{0.6}S_2$ from bulk probes to the local structure of Fe. We suggest that Al^{3+} stabilizes N by exerting electrostatic forces on the anion framework, preventing Fe from distorting within the FeS_4 tetrahedron. In the charged state, the isomer shift of $Li_{2.2}Al_{0.2}Fe_{0.6}S_2$ (0.330 ±0.080 mm/s) closely matches that of Li_2FeS_2 (0.339 ±0.083 mm/s), with N also showing slight distortion towards the base. This suggests that, once the capacity limit is reached at full charge, empty Fe-S $3d$-$3p$ states in both materials become similarly unstable.

Conclusion and outlook for excess $2\,S^{2-}/(S_2)^{2-}$ redox industrial element cathodes

The materials presented in this work offer new pathways towards next-generation Li-ion battery cathodes. Figure S23 compares the volumetric and gravimetric energy densities of various commercial and emerging state-of-the-art lithiated cathode materials with Li_2FeS_2 and $Li_{2.2}Al_{0.2}Fe_{0.6}S_2$. While $Li_{2.2}Al_{0.2}Fe_{0.6}S_2$ has a lower volumetric energy density than state-of-the-art oxides due to its larger sulfide anions, its gravimetric energy density surpasses all reported lithiated cathode materials. A very recent report shows that even highly optimized oxides, dubbed "integrated rocksalt-polyanion cathodes," can only match the energy density of $Li_{2.2}Al_{0.2}Fe_{0.6}S_2$ through overdischarge,[51] which, as we explain in the Introduction, is not scalable with current manufacturing techniques. $Li_{2.2}Al_{0.2}Fe_{0.6}S_2$ achieves this primarily through reversible redox of ≈80% of its anions with ≈100% Coulombic efficiency – the highest reported level of anion redox in a cathode material, exceeded only by conversion cathodes. The electrochemical performance of $Li_{2.2}Al_{0.2}Fe_{0.6}S_2$ paves the way for sulfides capable of high degrees of anion redox as high-performance cathodes composed of only the most industrial/scalable elements.

Substituting Al^{3+} into Li_2FeS_2 not only makes the material lighter, increasing gravimetric capacity, but also increases anion oxidation capacity in mole e^- per f.u. Anion oxidation capacity increases because Al^{3+} stabilizes the electrochemically oxidized material, which requires kinetic stabilization to prevent the formation of more thermodynamically stable products like pyrite FeS_2. We assess kinetic stability from electronic and structural perspectives. Electronically, we evaluate how Al^{3+} alters the propensity for S^{2-} to reduce $Fe^{\gtrsim 2.6+}$ in the electrochemically oxidized material. Upon annealing, oxidized Li_2FeS_2 shows Fe^{2+} formation through ligand to metal charge transfer that forms persulfides and pyrite FeS_2, whereas $Li_{2.2}Al_{0.2}Fe_{0.6}S_2$ shows Fe^{3+} reduction that preserves crystallinity without forming persulfides. This difference translates to more stable empty Fe-S $3d$-$3p$ states in deeply delithiated $Li_{2.2}Al_{0.2}Fe_{0.6}S_2$ than Li_2FeS_2, revealed by Mössbauer spectrometry. Structurally, Al^{3+} stabilizes the Fe local structure. Importantly, the introduction of Al expands the phase space of thermodynamically stable phases of the oxidized stoichiometries. Al_2FeS_4, for instance, is structurally very similar to $Li_{2.2}Al_{0.2}Fe_{0.6}S_2$ and therefore likely aids in the stability against conversion to pyrite. Thus, incorporating Al^{3+} addresses one of the key challenges in developing multielectron redox cathodes: stabilizing the highly delithiated state against phase transitions to more stable phases.

Methods

Materials preparation

All materials and precursors were handled inside an Ar-filled glovebox (H_2O and $O_2 \lesssim 1$ ppm). All $Li_{2+y}Al_yFe_{1-2y}S_2$ ($0 \leq y \leq 0.5$) materials were prepared by solid-state synthesis. Powders of Li_2S (Thermo Fisher Scientific, 99.9%), FeS (Sigma Aldrich, 99.9%), and Al_2S_3 (Thermo Fisher Scientific, 99+%) were weighed to an accuracy of ± 0.1 mg to give total 250 mg of a desired stoichiometry (i.e., value of y) and then hand-mixed in an agate mortar and pestle. The mixed precursor powders were pressed into $\frac{1}{4}$ inch diameter cylindrical pellets with a hand-operated arbor press. The mixed precursor pellets were light gray in color. Pellets were placed inside carbon-coated vitreous silica ampules (10 mm i.d., 12 mm o.d.), evacuated to $\leq$ 50 mTorr, and sealed with a methane-oxygen torch without exposure to air. The ampules were coated by first rinsing the inside of the empty ampule with acetone, and then pyrolyzing residual acetone with a methane-oxygen torch. The pyrolysis was repeated at least twice for conformal, continuous coating. The evacuated and sealed ampule was then placed inside a box furnace and heated at 1 °C/min to 900 °C with a dwell time of 12 h. After ambient cooling to room temperature (approximately 1 °C/min), the ampules were opened inside the glovebox and the pellets were ground into fine powders in agate mortar and pestles for further characterization. Only the $y = 0$ pellet melts into a polycrystalline boule when heated to 900 °C. The rest of the materials mostly retained the shape of the original pressed pellet. All products were black in both pellet and powder forms, except for $y = 0.4$ which is dark brown/red in powder form.

Synchrotron X-ray diffraction (sXRD) sample preparation

As prepared materials were packed into individual 1.0 mm (outer diameter) glass capillaries in an Ar-filled glovebox. Each capillary was evacuated to $\leq$ 50 mTorr and sealed with a methane-oxygen torch without exposing the sample to air. High-resolution sXRD patterns were collected on the sample-loaded capillaries at beamline 28-ID-1 (λ=0.1665 Å) at the National Synchrotron Light Source II at Brookhaven National Laboratory. The diffraction patterns were fit using the Rietveld method with the General Structure Analysis System II,[52] and crystal structures were visualized with VESTA.[53]

Inductively coupled plasma mass spectrometry (ICP-MS) and combustion analysis

ICP-MS was conducted at the Resnick Environmental Analysis Center at Caltech with an Agilent 8800 ICP-MS and argon plasma source. Roughly

3 mg of each synthesized batch of material was digested in 2 to 3 mL of concentrated HNO_3 (70 vol%) at 80 °C for 4 h. After the initial digestion, the solutions were twice diluted in dilute HNO_3 (5 vol%) to reach x2500 dilution. Final sample volumes were 25 mL. Standard solutions were prepared by diluting stock solutions of Li, Al, and Fe to the desired concentrations with dilute HNO_3 (5 vol%) to create a calibration curve.

Combustion analysis to quantify S content was conducted in duplicate for each sample by Atlantic Microlab (atlanticmicrolab.com). In an Ar-filled glovebox, roughly 10-15 mg of each sample was put into a 5 or 10 mL glass scintillation vial and the cap was sealed with electrical tape. The sample-loaded scintillation vials were sealed under Ar in aluminized mylar pouches (2 to 3 layers) using an impulse heat sealer (Uline) for shipping to Atlantic Microlab.

Freestanding cathode preparation

Freestanding cathodes were prepared by mixing 60/20/20 (wt%) active material, carbon (Super P, Alfa Aesar, >99%), and PTFE binder (Sigma, 1 μm powder), respectively, in agate mortar and pestles. The active material and carbon were mixed first, then binder was added to evenly distribute the active material and carbon in the binder framework. The hand grinding with binder creates small flakes ($\approx$1 mm^2) that were broken into smaller pieces/a powder by hand with a stainless steel spatula. Roughly 6 to 10 mg of the composite fragmented mix was weighed and pressed into a 6 mm diameter electrode under ca. 2 tons of force using a manual hydraulic press (Vivtek).

Electrochemical characterization

All electrochemical cells were assembled in an Ar-filled glovebox. Li-foil anodes with $\frac{1}{2}$ inch diameter were punched from either Li ribbon (Sigma, 99.9%, 0.75 mm) or Li chips (AOT Battery, 99.9%), both first mechanically cleaned with an Xacto blade immediately prior to cell assembly. The electrolyte, 1 M LP30, was a 1 M solution of $LiPF_6$ (Oakwood chemical, battery grade) in a 1/1 (by volume) mixture of ethylene carbonate (EC) and dimethyl carbonate (DMC), both Sigma, $\geq$99%.[54] The electrolyte was made (and stored) in an HDPE bottle by combining the carbonates and the salt, and was first stored at least overnight before use to ensure all components dissolved/mixed well. All electrochemistry was performed in 2032 coin cells (MTI) assembled with a stainless steel spring (MTI), stainless steel spacer (MTI), Li anode on the spacer, $\frac{1}{2}$ inch diameter glass-fiber separator (Whatman, GF/D), 100 μL of LP30 electrolyte (30 μL on the anode, 40 μL on the separator, 30 μL on the cathode), and freestanding cathode. All stainless steel coin cell components were sonicated in roughly 1/1 acetone/isopropyl alcohol for 30 minutes and then dried overnight in a vacuum oven at 60 °C prior to use in the glovebox. The glass fiber separators were dried overnight in a vacuum oven at 60 °C prior to use in the glovebox. The coin cells were crimped shut with a manual crimper (Pred Materials). All electrochemical experiments were performed with a BCS 805 battery cycler (Bio-Logic). For continuous galvanostatic cycling experiments, all materials were charged at a C/10 rate based on 1 e^- per f.u. up to 3 V, and discharged at the same rate to 1.7 V. For GITT experiments, currents were applied at the same C/10 rate for 20 minutes at a time separated by 4 hour rest periods. The equilibrium potential $V_{eq.}$ and overpotential η was extracted from the GITT using Python. The capacity fade rate (in % per cycle) for cycling at C/10 was determined by calculating linear fits of the average charge and discharge capacities versus cycle number of three replicate cells, then taking the slope over the value of the fit function at x=1 (cycle 1), and finally averaging this value for the charge and discharge fits. For the rate capability tests, the same charge/discharge voltage cut-offs of 3/1.7 V were used, and the cells were cycled for 5 cycles each, sequentially, at C/10, C/5, C/2, 1C, and back to C/10 (25 cycles total).

All *ex-situ* samples

All *ex-situ* samples were prepared in 2032 coin cells (MTI) with freestanding cathodes as previously described. Samples are first cycled to one of the following SOCs: mid-slope, transition, mid-plateau, charged, and discharged. For mid-slope samples, voltage cutoffs of $\approx$2.25 V for Li_2FeS_2 and $\approx$2.38 V for $Li_{2.2}Al_{0.2}Fe_{0.6}S_2$

were used. For transition samples, voltage cutoffs of ≈2.53 V for Li_2FeS_2 and ≈2.56 V for $Li_{2.2}Al_{0.2}Fe_{0.6}S_2$ were used. For mid-plateau samples, time cutoffs of ≈9.8 h for Li_2FeS_2 and ≈11.1 h for $Li_{2.2}Al_{0.2}Fe_{0.6}S_2$ were used. Due to slight cell-to-cell variation, cutoffs for these intermediate SOCs varied slightly and so for clarity are always shown with the full corresponding galvanostatic charge and discharge curves. For charged and discharged samples voltage cutoffs of 3 V and 1.7 V, respectively, were used. After cycling to one of the above-defined cutoffs, the cells were decrimped and opened with a manual disassembling tool (Pred Materials) in an Ar-filled glovebox. The *ex-situ* cathodes were gently scraped off the current collector by hand using a stainless steel spatula, keeping the cathode intact. Any visible glass fiber separator stuck on the cathode was manually scraped off the cathode surface with a stainless steel spatula. The cathodes were then immersed in ≈300 μL of DMC for 2-3 minutes to wash away residual electrolyte. The DMC was dabbed with a dry Kim wipe, which left minimal residual DMC, and then dried under vacuum for roughly 30 min. The dry intact cathodes were then either kept intact or broken into smaller pieces/a powder by hand with a stainless steel spatula, depending on the requirements of the subsequent characterization.

X-ray absorption spectroscopy (XAS)

Samples for *ex-situ* XAS were prepared in 2032 coin cells as previously described for *ex-situ* samples. The intact *ex-situ* cathodes, treated as previously described, were broken up into loose powders with a stainless steel spatula. All sample preparation described below was conducted in an Ar-filled glovebox. Prepared sample holders were sealed in Ar in aluminized mylar pouches (2 to 3 layers) using an impulse heat sealer (Uline) for transport to the respective synchrotrons. Calibration, background correction, and data processing of X-ray absorption near-edge structure was done in Athena from the IFEFIT suite.[55]

For Fe K-edge XAS, the loose powders were loaded into aluminum sample holders provided by the Stanford Synchrotron Radiation Lightsource (SSRL) at SLAC National Accelerator Laboratory, encapsulated between two pieces of Kapton tape (1 mil film thickness, 2.5 mil total thickness, Uline). All Fe K-edge XAS was measured in transmission mode at the SSRL at SLAC National Accelerator Laboratory. The Li_2FeS_2 data for the mid-slope and mid-plateau SOCs was measured at beamline 2-2. The rest of the data presented here was measured at beamline 4-3. In all cases, during measurement, the sample holder was placed in a continuous He-flushed chamber to minimize air exposure, and O_2 levels were measured to be ≈500 ppm with an O_2 sensor. Fe K-edge data were calibrated to a collinear Fe foil present for each sample. The data shown are three averaged sweeps of each sample, with each sweep taking roughly 20 minutes.

For S K-edge XAS, the loose powders were mixed by hand with agate mortar and pestles with boron nitride (BN) (Alfa Aesar, 99.5%) so that the total sample concentration was $\leq$5% by mass. Roughly 10 to 15 mg of each composite BN-sample mix was pressed into $\frac{1}{4}$ inch diameter pellets under roughly 1 ton of force in a hand-operated arbor press. The pellets were then loaded into plastic sample holders provided by the National Synchrotron Light Source II (NSLS-II) at Brookhaven National Laboratory (BNL), sandwiched between a polypropylene layer and Kapton tape and adhered to the sample holder using Kapton tape. S K-edge XAS was measured in fluorescence mode at beamline 8-BM at NSLS-II at BNL. During measurement, the sample holder was placed in a continuous He-flushed chamber to minimize air exposure. S K-edge data were calibrated to a gypsum, i.e., sulfate S^{6+}, standard (1 wt% $CaSO_4 \cdot 2\,H_2O$ in polyethylene glycol). The data shown are three averaged sweeps of each sample, with each sweep taking roughly 15 minutes.

CuK_α XRD

CuK_α XRD patterns were collected on a Rigaku SmartLab diffractometer. To prevent air exposure during measurement, samples were loaded inside an Ar-filled glovebox into a Rigaku-built air-free sample holder with a low background silicon sample platform. For synthesized materials, roughly 10 mg of sample powder was placed and compressed (by hand using a stainless steel spatula) onto the sample platform. For ex – situ cath-

odes, the cathode was kept intact and gently placed onto the sample platform. The diffraction patterns were fit using the Rietveld method with the General Structure Analysis System II (GSAS-II)[52] and crystal structures were visualized with VESTA.[53]

Synthesis of $Al_{0.2}Fe_{0.6}S_2$

The material and precursors were handled in an Ar-filled glovebox. Powders of Al (Alfa Aesar, 99.5%), Fe (Acros Organics, 99.0%), and S_8 (Acros Organics, >99.5%) were weighed to an accuracy of ± 0.1 mg to give total 250 mg of $Al_{0.2}Fe_{0.6}S_2$ and then hand-mixed in an agate mortar and pestle. The mixed precursor powders were pressed into $\frac{1}{4}$ inch diameter cylindrical pellets with a hand-operated arbor press. The mixed precursor pellet was gray in color. The pellet was placed inside a vitreous silica ampule (10 mm i.d., 12 mm o.d.), evacuated to ≤ 50 mTorr, and sealed with a methane-oxygen torch without exposure to air. The evacuated and sealed ampule was then placed inside a box furnace and heated at 1 °C/min to 900 °C with a dwell time of 12 h. After ambient cooling to room temperature (roughly at a rate of 1 °C/min), the ampule was opened inside the glovebox. The pellet after heating was a glittery dark gray color and fully melted, conforming to the shape of the ampule with slight bright yellow S residue stuck to the sides of the ampule.

Ex-situ annealing and resting

For annealing and resting experiments, the cathode was first charged to the transition SOC. The cell was then stopped and disassembled in an Ar-filled glovebox, and the cathode was removed and rinsed as previously described. The intact cathode was then placed in vitreous silica ampules (10 mm i.d., 12 mm o.d.), evacuated to ≤ 50 mTorr, and sealed with a methane-oxygen torch without exposure to air. For annealing experiments, the cathode in the evacuated ampule was placed inside a box furnace and then heated at 1 °C/min to 200 °C, then annealed at 200 °C for 2 hours, and then ambiently cooled to room temperature by shutting off the furnace. For resting experiments, the cathode in the evacuated ampule was kept at room temperature for ≈1 week. The ampule containing the annealed or rested cathode was then opened inside an Ar-filled glovebox, and a new cell was assembled as previously described with the annealed or rested cathode.

Mössbauer sample preparation and measurement

Ex-situ samples for Mössbauer spectrometry were initially prepared as previously described. The cathode was kept intact and placed on a small piece of Kapton tape (1 mil film thickness, 2.5 mil total thickness, Uline). The Kapton tape was adhered to the inside of a static shielding bag (3 mil thickness, Uline) and sealed in Ar with an impulse heat sealer (Uline). The cathode itself is ≈100 μm thick. The sample, sealed in the bag, was encapsulated between Pb apertures with 5.5 mm openings to prevent excess background γ rays from reaching the Mössbauer detector, and held in place with Scotch tape such that the 5.5 mm hole revealed only the cathode. The Mössbauer spectra were acquired at room temperature, in transmission geometry, in the constant acceleration mode of a Wissel 1200 spectrometer and with a ^{57}Co(Rh) γ-ray source (Ritverc MCo7.123) with an activity of ≈19 mCi. The thickness of the samples (in mg of natural Fe per cm^2) was about 3 to 4.4 mg·cm^{-2}. The velocity scale ($\pm$3 mm/s) was calibrated at room temperature with a 30 μm thick α-Fe foil (99.99+% purity). Each spectrum was acquired for ≈24 hours.

Mössbauer fitting

We use the MossA program to fit the Mössbauer spectra.[56] We show the Mössbauer spectra of Li_2FeS_2 and $Li_{2.2}Al_{0.2}Fe_{0.6}S_2$ at each SOC in Figure S15 and Figure S16, respectively. Each spectrum is shown with the accompanying fit, each fit component/Fe site, and difference between the fit and the data. Each spectrum is fit with four symmetric Lorentzian doublets representing four separate Fe sites. Each doublet has four fit parameters: (1) the isomer shift , the center point between the two peaks of the doublet, (2) the quadrupole splitting, the separation between the peaks, (3) the peak full width half maximum/the

linewidth (Γ), and (4) the percent area value (related to the peak intensity scaled by $\pi\Gamma$). The fitted values of all parameters for each spectrum are tabulated in Table S6. We use 4 separate Fe sites to achieve realistic linewidths for each Lorentzian doublet fit component and to reflect the actual variety of the possible coordination environments of Fe in the materials. We use a nested configuration of the Lorentzian doublets in our fits where possible, over a staggered configuration, as the nested fit better reflects the electron delocalization we expect in the materials.[57] In every fit, we constrain the linewidths of all doublets to be equal in order to reduce free parameters and simplify interpretation. We verify the isomer shift trends from our fits using spectral centroid analysis. The centroids of the spectra in Figures S15 and S16 are calculated as: centroid $= \frac{\sum_i I(v_i)\cdot v_i}{\sum_i I(v_i)}$, where $I(v_i)$ is the normalized absorption intensity, v_i is the velocity, and i indexes the data points. The centroids are shown in Figure S22 with the isomer shift data. Since the centroids are calculated directly from the raw data without fitting parameters, they provide direct access to the isomer shift. They follow the same trend as the weighted average isomer shifts from our fits, confirming that the fits accurately represent the data and are unbiased.

Fe K-edge EXAFS fitting

We use the Athena and Artemis software from the IFEFIT suite for Fe K-edge EXAFS fitting.[55] In Fe K-edge XAS, oscillations at energies beyond the primary electronic transition arise from the interference of the excited photoelectron with itself after scattering off neighboring atoms.[58] The oscillations are converted to a function of the wave number, $\chi(k)$, which is then Fourier transformed to real space ($|\chi(R)|$). The $\chi(k)$ are fit within a k window of roughly $\approx$3.0$\pm$0.1 to $\approx$10$\pm$1 Å^{-1} (sample dependent), with dk=2 Å^{-1}. The $|\chi(R)|$ are fit within an R window of roughly $\approx$1.1$\pm$0.1 to $\approx$10 Å (sample dependent), with dR=0.2 Å. The amplitude reduction factor S_0^2 is held fixed for all *ex-situ* samples and is determined by fitting the first shell of the $\chi(k)$ and $|\chi(R)|$ of the Fe calibration foil, using a k window of 5 to 11 Å^{-1} (dk = 2 Å^{-1}) and R window of 1 to 3 Å (dR = 2 Å). The intensity of the Fourier transform, $|\chi(R)|$, represents the oscillation intensity in real space, corresponding to correlation shells, with Fe located at 0 Å. We fit the first and second shell correlations with defined scattering paths and determine the correlation distance, $r_{eff.}$ (Å), and the coordination number N. The first shell describes the immediate coordination of Fe by S, and the second shell describes the nearest neighbor cations at the edge-sharing tetrahedral sites closest to a given Fe. For Li_2FeS_2, we model the second shell with only Fe, as the scattering probability off of Li^+ is very low because of its small electron cloud. For $Li_{2.2}Al_{0.2}Fe_{0.6}S_2$, although the Al^{3+} electron cloud is nonnegligible, we still model the second shell with only Fe because the low Al content (0.2 mole Al^{3+} per f.u.) minimizes the scattering probability. The EXAFS analysis is conducted at all of the previously described SOCs. The resolution of our EXAFS data (the oscillations $\gtrapprox$50 eV above the rising edge), limits us to fitting both the first and second shells using only single scattering paths. This captures overall changes but not specific atomic positions or heterogeneity thereof. For example, the first shell actually includes 4 separate S atoms, each with its own scattering path, but we fit the first shell with a single scattering path, capturing the average effect of the multiple S atoms through the coordination number N. The EXAFS first and second shell $r_{\text{eff.}}$ and N are shown in Figure S17, with the fitted $\chi(k)$ and $|\chi(R)|$ in Figures S18 and S19 and Figures S20 and S21, respectively, and all fit parameters in Table S7.

Acknowledgments

This material is based upon work supported by the National Science Foundation (NSF) under Award No. DMR-2340864. K.A.S. acknowledges support from the Packard Fellowship for Science and Engineering, the Alfred P. Sloan Foundation, and the Camille and Henry Dreyfus Foundation. E.S.P. acknowledges support from the Robert and Patricia Switzer Foundation. E.S.P., M.D.Q., and C.T.M. acknowledge NSF Graduate Research Fellowship support under Award No. DGE-2139433. B.F. and P.G. acknowledge support from NSF Award No. DMR-1904714. Initial work on this material was partially supported by the Center

for Synthetic Control Across Length-scales for Advancing Rechargeables (SCALAR), an Energy Frontier Research Center funded by the U.S. Department of Energy, Office of Science, Basic Energy Sciences under award no. DE-SC0019381. This research used beam lines 2-2 and 4-3 at the Stanford Synchrotron Radiation Lightsource (SSRL). Use of SSRL, SLAC National Accelerator Laboratory, is supported by the U.S. Department of Energy, Office of Science, Office of Basic Energy Sciences under Contract No. DE-AC02-76SF00515. This research used beam lines 8-BM and 28-ID-1 of the National Synchrotron Light Source II (NSLS-II), a U.S. Department of Energy (DOE) Office of Science User Facility operated for the DOE Office of Science by Brookhaven National Laboratory (BNL) under Contract No. DE-SC0012704. The authors thank the Resnick Environmental Analysis Center at Caltech for ICP-MS and the Beckman Institute and Caltech X-ray Crystallography Facility for CuK_α XRD. The authors also thank Dr. Yonghua Du and Dr. Sarah Nicholas at 8-BM (NSLS-II) for their assistance with S K-edge XAS, Dr. Gihan Kwon at 28-ID-1 (NSLS-II) for his help with sXRD, and Dr. Erik Nelson and Dr. Matthew Latimer at 2-2 and 4-3 (SSRL) for their help with Fe K-edge XAS. The authors lastly thank Dr. Joshua J. Zak and Dr. Zachery W. B. Iton for their feedback and insights.

References

(1) *Net Zero by 2050 – A Roadmap for the Global Energy Sector*; 2021.

(2) Armstrong, R.; Chiang, Y.-M.; Gruenspecht, H. *The Future of Energy Storage*; MIT Future Of; 2022.

(3) *Net Zero 2050 and the Battery Arms Race*; 2023.

(4) Frith, J. T.; Lacey, M. J.; Ulissi, U. A Non-Academic Perspective on the Future of Lithium-Based Batteries. *Nature Communications* **2023**, *14*, 420.

(5) More Phosphoric Acid Refining Capacity Needed as LFP Demand Increases. https://source.benchmarkminerals.com/article/more-phosphoric-acid-refining-capacity-needed-as-lfp-demand-increases, 2023.

(6) *Mineral Commodity Summaries 2024*; USGS Numbered Series 2024, 2024.

(7) Putsche, V. L.; Pattany, J.; Ghosh, T.; Atnoorkar, S.; Zuboy, J.; Carpenter, A.; Takeuchi, E. S.; Marschilok, A. C.; Takeuchi, K. J.; Burrell, A.; Mann, M. K. A Framework for Integrating Supply Chain, Environmental, and Social Justice Factors during Early Stationary Battery Research. *Frontiers in Sustainability* **2023**, *4*.

(8) Duffner, F.; Kronemeyer, N.; Tübke, J.; Leker, J.; Winter, M.; Schmuch, R. Post-Lithium-Ion Battery Cell Production and Its Compatibility with Lithium-Ion Cell Production Infrastructure. *Nature Energy* **2021**, *6*, 123–134.

(9) Degen, F.; Winter, M.; Bendig, D.; Tübke, J. Energy Consumption of Current and Future Production of Lithium-Ion and Post Lithium-Ion Battery Cells. *Nature Energy* **2023**, *8*, 1284–1295.

(10) LFP 2.0 Is Not about the Price of Lithium, Here's What's Driving Demand. https://source.benchmarkminerals.com/article/lfp-2-0-is-not-about-the-price-of-lithium-heres-whats-driving-demand, 2020.

(11) Yamada, A.; Chung, S. C.; Hinokuma, K. Optimized LiFePO4 for Lithium Battery Cathodes. *Journal of The Electrochemical Society* **2001**, *148*, A224.

(12) Manthiram, A.; Song, B.; Li, W. A Perspective on Nickel-Rich Layered Oxide Cathodes for Lithium-Ion Batteries. *Energy Storage Materials* **2017**, *6*, 125–139.

(13) Melot, B. C.; Scanlon, D. O.; Reynaud, M.; Rousse, G.; Chotard, J.-N.; Henry, M.; Tarascon, J.-M. Chemical and Structural Indicators for Large Redox Potentials in Fe-Based Positive Electrode Materials. *ACS Applied Materials & Interfaces* **2014**, *6*, 10832–10839.

(14) Ati, M.; Melot, B. C.; Chotard, J. N.; Rousse, G.; Reynaud, M.; Tarascon, J. M. Synthesis and Electrochemical Properties of Pure LiFeSO4F in the *Triplite* Structure. *Electrochemistry Communications* **2011**, *13*, 1280–1283.

(15) Rousse, G.; Tarascon, J. M. Sulfate-Based Polyanionic Compounds for Li-Ion Batteries: Synthesis, Crystal Chemistry, and Electrochemistry Aspects. *Chemistry of Materials* **2014**, *26*, 394–406.

(16) Heo, J.; Jung, S.-K.; Hwang, I.; Cho, S.-P.; Eum, D.; Park, H.; Song, J.-H.; Yu, S.; Oh, K.; Kwon, G.; Hwang, T.; Ko, K.-H.; Kang, K. Amorphous Iron Fluorosulfate as a High-Capacity Cathode Utilizing Combined Intercalation and Conversion Reactions with Unexpectedly High Reversibility. *Nature Energy* **2023**, *8*, 30–39.

(17) Zak, J. J.; Kim, S. S.; Laskowski, F. A. L.; See, K. A. An Exploration of Sulfur Redox in Lithium Battery Cathodes. *Journal of the American Chemical Society* **2022**, *144*, 10119–10132.

(18) Zhang, M.; Kitchaev, D. A.; Lebens-Higgins, Z.; Vinckeviciute, J.; Zuba, M.; Reeves, P. J.; Grey, C. P.; Whittingham, M. S.; Piper, L. F. J.; Van der Ven, A.;

Meng, Y. S. Pushing the Limit of 3d Transition Metal-Based Layered Oxides That Use Both Cation and Anion Redox for Energy Storage. *Nature Reviews Materials* **2022**, *7*, 522–540.

(19) Ogley, M. J. W. et al. Metal–Ligand Redox in Layered Oxide Cathodes for Li-ion Batteries. 2024.

(20) Hong, J. et al. Metal–Oxygen Decoordination Stabilizes Anion Redox in Li-rich Oxides. *Nature Materials* **2019**, *18*, 256–265.

(21) Li, B.; Sougrati, M. T.; Rousse, G.; Morozov, A. V.; Dedryvère, R.; Iadecola, A.; Senyshyn, A.; Zhang, L.; Abakumov, A. M.; Doublet, M.-L.; Tarascon, J.-M. Correlating Ligand-to-Metal Charge Transfer with Voltage Hysteresis in a Li-rich Rock-Salt Compound Exhibiting Anionic Redox. *Nature Chemistry* **2021**, *13*, 1070–1080.

(22) Kim, S. S.; Agyeman-Budu, D. N.; Zak, J. J.; Andrews, J. L.; Li, J.; Melot, B. C.; Nelson Weker, J.; See, K. A. Effect of Metal d Band Position on Anion Redox in Alkali-Rich Sulfides. *Chemistry of Materials* **2024**,

(23) Kim, S. S.; Kitchaev, D. A.; Patheria, E. S.; Morrell, C. T.; Qian, M. D.; Andrews, J. L.; Yan, Q.; Ko, S.-T.; Luo, J.; Melot, B. C.; Van der Ven, A.; See, K. A. Cation Vacancies Enable Anion Redox in Li Cathodes. *Journal of the American Chemical Society* **2024**,

(24) McCalla, E.; Sougrati, M. T.; Rousse, G.; Berg, E. J.; Abakumov, A.; Recham, N.; Ramesha, K.; Sathiya, M.; Dominko, R.; Van Tendeloo, G.; Novák, P.; Tarascon, J.-M. Understanding the Roles of Anionic Redox and Oxygen Release during Electrochemical Cycling of Lithium-Rich Layered Li4FeSbO6. *Journal of the American Chemical Society* **2015**, *137*, 4804–4814.

(25) House, R. A.; Marie, J.-J.; Pérez-Osorio, M. A.; Rees, G. J.; Boivin, E.; Bruce, P. G. The Role of O2 in O-redox Cathodes for Li-ion Batteries. *Nature Energy* **2021**, *6*, 781–789.

(26) Li, B.; Kumar, K.; Roy, I.; Morozov, A. V.; Emelyanova, O. V.; Zhang, L.; Koç, T.; Belin, S.; Cabana, J.; Dedryvère, R.; Abakumov, A. M.; Tarascon, J.-M. Capturing Dynamic Ligand-to-Metal Charge Transfer with a Long-Lived Cationic Intermediate for Anionic Redox. *Nature Materials* **2022**, 1–10.

(27) Zak, J. J.; Zuba, M.; Lebens-Higgins, Z. W.; Huang, H.; Crafton, M. J.; Dalleska, N. F.; McCloskey, B. D.; Piper, L. F. J.; See, K. A. Irreversible Anion Oxidation Leads to Dynamic Charge Compensation in the Ru-Poor, Li-Rich Cathode Li2Ru0.3Mn0.7O3. *ACS Energy Letters* **2023**, *8*, 722–730.

(28) Saha, S.; Assat, G.; Sougrati, M. T.; Foix, D.; Li, H.; Vergnet, J.; Turi, S.; Ha, Y.; Yang, W.; Cabana, J.; Rousse, G.; Abakumov, A. M.; Tarascon, J.-M. Exploring the Bottlenecks of Anionic Redox in Li-rich Layered Sulfides. *Nature Energy* **2019**, *4*, 977–987.

(29) Batchelor, R. J.; Einstein, F. W. B.; Jones, C. H. W.; Fong, R.; Dahn, J. R. Crystal Structure of ${\mathrm{Li}}_{2}$${\mathrm{FeS}}_{2}$. *Physical Review B* **1988**, *37*, 3699–3702.

(30) Hansen, C. J.; Zak, J. J.; Martinolich, A. J.; Ko, J. S.; Bashian, N. H.; Kaboudvand, F.; Van der Ven, A.; Melot, B. C.; Nelson Weker, J.; See, K. A. Multielectron, Cation and Anion Redox in Lithium-Rich Iron Sulfide Cathodes. *Journal of the American Chemical Society* **2020**, *142*, 6737–6749.

(31) Lim, H.; Kim, S.-C.; Kim, J.; Kim, Y.-I.; Kim, S.-J. Structure of Li5AlS4 and Comparison with Other Lithium-Containing Metal Sulfides. *Journal of Solid State Chemistry* **2018**, *257*, 19–25.

(32) Leube, B. T.; Inglis, K. K.; Carrington, E. J.; Sharp, P. M.; Shin, J. F.; Neale, A. R.; Manning, T. D.; Pitcher, M. J.; Hardwick, L. J.; Dyer, M. S.; Blanc, F.; Claridge, J. B.; Rosseinsky, M. J. Lithium Transport in Li4.4M0.4M′0.6S4 (M = Al3+, Ga3+, and M′ = Ge4+, Sn4+): Combined Crystallographic, Conductivity, Solid State NMR, and

Computational Studies. *Chemistry of Materials* **2018**, *30*, 7183–7200.

(33) Gamon, J.; Duff, B. B.; Dyer, M. S.; Collins, C.; Daniels, L. M.; Surta, T. W.; Sharp, P. M.; Gaultois, M. W.; Blanc, F.; Claridge, J. B.; Rosseinsky, M. J. Computationally Guided Discovery of the Sulfide Li3AlS3 in the Li–Al–S Phase Field: Structure and Lithium Conductivity. *Chemistry of Materials* **2019**, *31*, 9699–9714.

(34) Gamon, J.; Dyer, M. S.; Duff, B. B.; Vasylenko, A.; Daniels, L. M.; Zanella, M.; Gaultois, M. W.; Blanc, F.; Claridge, J. B.; Rosseinsky, M. J. Li4.3AlS3.3Cl0.7: A Sulfide–Chloride Lithium Ion Conductor with Highly Disordered Structure and Increased Conductivity. *Chemistry of Materials* **2021**, *33*, 8733–8744.

(35) Fasiska, E. J. Some Defect Structures of Iron Sulfide. *physica status solidi (a)* **1972**, *10*, 169–173.

(36) Baker, M. L.; Mara, M. W.; Yan, J. J.; Hodgson, K. O.; Hedman, B.; Solomon, E. I. K- and L-edge X-ray Absorption Spectroscopy (XAS) and Resonant Inelastic X-ray Scattering (RIXS) Determination of Differential Orbital Covalency (DOC) of Transition Metal Sites. *Coordination Chemistry Reviews* **2017**, *345*, 182–208.

(37) Glaser, T.; Hedman, B.; Hodgson, K. O.; Solomon, E. I. Ligand K-Edge X-ray Absorption Spectroscopy: A Direct Probe of Ligand-Metal Covalency. *Accounts of Chemical Research* **2000**, *33*, 859–868.

(38) Tokuda, M.; Yoshiasa, A.; Mashimo, T.; Arima, H.; Hongu, H.; Tobase, T.; Nakatsuka, A.; Sugiyama, K. Crystal Structure Refinement of MnTe2, MnSe2, and MnS2: Cation-Anion and Anion–Anion Bonding Distances in Pyrite-Type Structures. *Zeitschrift für Kristallographie - Crystalline Materials* **2019**, *234*, 371–377.

(39) Fleet, M. E. The Crystal Structure of a Pyrrhotite (Fe7S8). *Acta Crystallographica Section B: Structural Crystallography and Crystal Chemistry* **1971**, *27*, 1864–1867.

(40) Nishida, K.; Narita, T. Some Experiments on the Formation of an Fe-Al Double Sulfide Compound. *Bulletin of the Faculty of Engineering, Hokkaido University* **1976**, *81*, 99–109.

(41) Menard, M. C.; Ishii, R.; Higo, T.; Nishibori, E.; Sawa, H.; Nakatsuji, S.; Chan, J. Y. High-Resolution Synchrotron Studies and Magnetic Properties of Frustrated Antiferromagnets MAl2S4 (M = Mn2+, Fe2+, Co2+). *Chemistry of Materials* **2011**, *23*, 3086–3094.

(42) Verchenko, V. Y.; Kanibolotskiy, A. V.; Bogach, A. V.; Znamenkov, K. O.; Shevelkov, A. V. Ferromagnetic Correlations in the Layered van Der Waals Sulfide FeAl2S4. *Dalton Transactions* **2022**, *51*, 8454–8460.

(43) Bin, M.; Pauthenet, R. Magnetic Anisotropy in Pyrrhotite. *Journal of Applied Physics* **1963**, *34*, 1161–1162.

(44) Gosselin, J. R.; Townsend, M. G.; Tremblay, R. J.; Webster, A. H. Mössbauer Investigation of Synthetic Single Crystal Monoclinic Fe7S8. *Materials Research Bulletin* **1975**, *10*, 41–49.

(45) Levinson, L. M.; Treves, D. Mössbauer Study of the Magnetic Structure of Fe7S8. *Journal of Physics and Chemistry of Solids* **1968**, *29*, 2227–2231.

(46) Shimada, K.; Mizokawa, T.; Mamiya, K.; Saitoh, T.; Fujimori, A.; Ono, K.; Kakizaki, A.; Ishii, T.; Shirai, M.; Kamimura, T. Spin-Integrated and Spin-Resolved Photoemission Study of Fe Chalcogenides. *Physical Review B* **1998**, *57*, 8845–8853.

(47) Blandeau, L.; Ouvrard, G.; Calage, Y.; Brec, R.; Rouxel, J. Transition-Metal Dichalcogenides from Disintercalation Processes. Crystal Structure Determination and Mossbauer Study of Li2FeS2 and Its Disintercalates LixFeS2 ($0.2 \leq x \leq 2$). *Journal*

of Physics C: Solid State Physics **1987**, *20*, 4271.

(48) Goodenough, J. B.; Fatseas, G. Mössbauer 57Fe Isomer Shift as a Measure of Valence in Mixed-Valence Iron Sulfides. *Journal of Solid State Chemistry* **1982**, *41*, 1–22.

(49) Parish, R. V. In *Mössbauer Spectroscopy*; Dickson, D. P. E., Berry, F. J., Eds.; Cambridge University Press: Cambridge, 1986; pp 17–69.

(50) Fultz, B. *Characterization of Materials*; John Wiley & Sons, Ltd: New York, NY, 2011.

(51) Huang, Y. et al. Integrated Rocksalt–Polyanion Cathodes with Excess Lithium and Stabilized Cycling. *Nature Energy* **2024**, 1–9.

(52) Toby, B. H.; Von Dreele, R. B. GSAS-II: The Genesis of a Modern Open-Source All Purpose Crystallography Software Package. *Journal of Applied Crystallography* **2013**, *46*, 544–549.

(53) Momma, K.; Izumi, F. VESTA 3 for Three-Dimensional Visualization of Crystal, Volumetric and Morphology Data. *Journal of Applied Crystallography* **2011**, *44*, 1272–1276.

(54) Tarascon, J. M.; Guyomard, D. New Electrolyte Compositions Stable over the 0 to 5 V Voltage Range and Compatible with the Li1+xMn2O4/Carbon Li-ion Cells. *Solid State Ionics* **1994**, *69*, 293–305.

(55) Ravel, B.; Newville, M. ATHENA, ARTEMIS, HEPHAESTUS: Data Analysis for X-ray Absorption Spectroscopy Using IFEFFIT. *Journal of Synchrotron Radiation* **2005**, *12*, 537–541.

(56) Prescher, C.; McCammon, C.; Dubrovinsky, L. MossA: A Program for Analyzing Energy-Domain Mössbauer Spectra from Conventional and Synchrotron Sources. *Journal of Applied Crystallography* **2012**, *45*, 329–331.

(57) Brown, A. C.; Thompson, N. B.; Suess, D. L. M. Evidence for Low-Valent Electronic Configurations in Iron–Sulfur Clusters. *Journal of the American Chemical Society* **2022**, *144*, 9066–9073.

(58) Newville, M. Fundamentals of XAFS. *Reviews in Mineralogy and Geochemistry* **2014**, *78*, 33–74.